Rock Mechanics and Rock Engineering (2020) 53:3983–4000
https://doi.org/10.1007/s00603-020-02162-8

ORIGINAL PAPER

Low-Amplitude Wave Propagation and Attenuation Through Damaged Rock and a Classification Scheme for Rock Fracturing Degree

Jianbo Zhu[1,2] · Tianqi Zhai[1] · Zhiyi Liao[2] · Shengqi Yang[3] · Xiaoli Liu[4] · Tao Zhou[2]

Received: 8 October 2019 / Accepted: 26 May 2020 / Published online: 10 June 2020

Abstract

Damaged rock mass contains a great number of microstructures and defects at various scales, which could influence wave propagation significantly. In this paper, investigation of low-amplitude stress wave attenuation in rocks with different damage degrees was undertaken to determine the effects of parameters including damage degree, heterogeneity and type of waveforms on wave propagation, attenuation and slowness. The numerical method was validated through comparison with laboratory measurements. The damage was induced by conducting uniaxial compression tests on the intact rocks and was defined with the acoustic emission. The results showed that the attenuation ratio of low-amplitude stress wave increases with increasing rock damage degree. The rock heterogeneity was incorporated into the numerical model using a digital image processing technique with the combination of X-ray micro-computerized tomography. We found that the rock heterogeneity has great influence on the wave amplitude attenuation. Three types of waveforms, i.e., half-sine wave, square wave and exponential decay wave, were utilized to analyze influences of waveforms on attenuation characteristics in damaged rock specimens. The attenuation ratio of the exponential decay wave is the highest for rock specimens with the same damage degree, attributed to its highest dominant frequency. Moreover, detailed spectrum analysis suggested that the dominant frequency of the wave signal decreases with increasing damage degree. Based on derived simulating results, an improved classification scheme for determining rock fracturing degree, which groups the rock into zones of slightly fractures, moderately fractured and strongly fractured, was established by considering the relationship between wave amplitude and damage, since wave amplitude, other than wave velocity, is more sensitive to rock damage. The findings in this paper could facilitate a better understanding of wave propagation through rock and provide another means to determine rock fracturing degree.

Keywords Wave propagation · Rock damage · Rock fracturing degree · Heterogeneity

1 Introduction

Rock material is a heterogeneous and anisotropic compound structure, containing many discontinuities, such as voids, fissures and joints. The growth and extension of these discontinuities under the external load or during geological process are identified as the evolution of damage in continuum damage mechanics (Kachanov and Krajcinovic 1986). The existence of these damages could notably affect wave propagation and attenuation in rocks. Therefore, it is of great significance to understand stress wave propagation and attenuation through damaged rock (Xie et al. 2020).

Continuum damage mechanics use internal state variables to correlate the microdefects to the macroscopic material properties. A reasonable definition of damage variables is the focus of this theory and has been discussed widely. Whether based on the physical meaning of damage under

✉ Jianbo Zhu
jbzhu@tju.edu.cn
http://jgxy.tju.edu.cn/teachers.asp?id=256

[1] State Key Laboratory of Hydraulic Engineering Simulation and Safety, School of Civil Engineering, Tianjin University, Tianjin, China

[2] Guangdong Provincial Key Laboratory of Deep Earth Sciences and Geothermal Energy Exploitation and Utilization, Institute of Deep Earth Sciences and Green Energy, College of Civil and Transportation Engineering, Shenzhen University, Shenzhen, China

[3] State Key Laboratory for Geomechanics and Deep Underground Engineering, School of Mechanics and Civil Engineering, China University of Mining and Technology, Xuzhou, China

[4] State Key Laboratory of Hydroscience and Engineering, Tsinghua University, Beijing, China

a continuity assumption or based on test operability, there have been many proposed methods to calculate and evaluate damage evolution of brittle materials quantitatively. As a straightforward extension of Kachanov's concept of damage (Kachanov and Krajcinovic 1986), Lemaitre and Chaboche (1994) defined an isotropic damage model by the effective elastic modulus. Taylor et al. (1986) and Kuszmaul (1987) defined the crack density as the damage variable. The acoustic emission (AE) events that are related to the development of fractures and the spatial evolution of microcracks (Lei et al. 2004; Yang and Jing 2011) also have been used to define material damage (Tang et al. 1997; Tuffen et al. 2008). With the application of X-ray computed tomography (CT) in solid mechanics, the CT value of the scanned images can be adopted to characterize damage evolution of rocks quantitatively during loading or unloading (Ma et al. 2016; Duan et al. 2019). Although the application of damage mechanics into rock materials needs to be explored further, the abovementioned definition methods and corresponding damage evolution models have made outstanding contributions to the understanding of rock failure.

Wave propagation and attenuation in rock has received considerable attentions (Moustachi and Thimus 1997; Persson 1997; Cadoret et al. 1998; Zhao and Cai 2001; Li 2013; Li et al. 2014, 2015, 2017a). Moustachi and Thimus (1997) suggested that the propagation of stress waves in natural media can be characterized by their velocity and attenuation. The wave attenuation in various rock materials, such as limestone (Cadoret et al. 1998), sandstone (Xue et al. 2013) and coal (Feng et al. 2016), has been investigated extensively in the laboratory. The mechanical behavior of joints in rocks and their effects on wave propagation are also investigated by theoretical or experimental methods (Zhao and Cai 2001; Zhu et al. 2019). Variations of wave-related parameters, such as particle peak velocity, are adopted to evaluate the degree of rock damage (Persson 1997). Ultrasonic pulse velocity could be used conveniently for nondestructive testing of the physical and mechanical properties of materials and structures, and the wave velocity slowness indicates increasing damage inside the structure (Carpinteri and Lacidogna 2007; Faella et al. 2012). The dominant frequency was used to evaluate the stress wave propagation through rock (Fan and Wu 2016). More laboratory tests examining the cracks or joints in rock materials (Huang et al. 2014; Yang et al. 2019) or concrete strength (Akkaya et al. 2003) are based on nondestructive low-amplitude wave propagation.

With advances in computer technology, various numerical methods have been developed to date to investigate the effects of the microdefects or joints on wave attenuation in rocks. Wang et al. (2008) studied blast-induced wave propagation and spalling in rock based on the finite element method. Zhu and Tang (2006) studied the failure of rocks under dynamic impact. Bansal et al. (2008) modeled S-wave splitting in anisotropic media with finite difference method. Huang et al. (2015) conducted a numerical simulation of stress wave propagation through filled joints by a particle model. Wave attenuation with considerations of discontinuous deformation in rock was studied by Gu and Zhao (2010). Wave transmission across jointed rock masses was investigated by Zhu et al. (2013) with a universal distinct element code. However, most previous studies were focused on intact rock or jointed rock mass; the understanding of wave propagation across damaged rock is still at its infancy.

Numerical models were established by a FEM-based programme Rock Failure Process Analysis (RFPA) in this study to investigate the relationship between rock damage and wave attenuation, especially the effect of damage degree, rock heterogeneity and waveform on wave propagation. Low-amplitude stress waves were loaded on models with different degrees of damage, where the damage was generated by static compression. The wave amplitude and wave velocity were employed to characterize the attenuation of the wave in the damaged rock. The digital image processing (DIP) technique was employed to establish different types of rock models to analyze the influence of rock heterogeneity on wave attenuation. After validation of the numerical method through comparison with laboratory measurement, three different incident waveforms were loaded in the same model to study the effect of waveform on wave attenuation. In addition, using the simulation results, an improved rock quality classification chart based on the relationship between damage and wave amplitude attenuation was established. This study is helpful for better understanding of the relationship between damage evolution and wave attenuation in rocks, and is significant for rock damage detection.

2 Numerical Model and Methods

2.1 Implement of Rock Heterogeneity in RFPA

Rock material generally is considered to be heterogeneous, discontinuous and anisotropic. The mechanical behavior of rock varies significantly on account of grain-scale heterogeneity (Li et al. 2017b). To describe the heterogeneous behavior of rock, the mechanical parameters of elements are assumed to follow the Weibull distribution (Weibull 1951), which is expressed as

$$\varphi(x) = \frac{m}{x_0}\left(\frac{x}{x_0}\right)^{m-1} \exp\left(-\left(\frac{x}{x_0}\right)^{m}\right), \tag{1}$$

where x is a certain variable such as elasticity modulus, strength or density, x_0 is the corresponding mean value of the whole elements, and m defines the shape of the distribution function representing the degree of material homogeneity, and has been widely called the homogeneity index (Tang 1997, Liao et al. 2016). The material is more homogeneous when the value of m is greater.

2.2 Definition of Damage of Rock Sample

Kachanov and Krajcinovic (1986) defined the damage as:

$$D_s = \frac{A_d}{A}, \tag{2}$$

where D_s refers to the macroscopic damage of the rock sample, A_d is the damaged area and A is the area of overall cross section. Tang (1997) suggested that if the constitutive law of elements before damage is linearly elastic, the energy in an element will be released as elastic energy when it fails. Hence, in RFPA code, one AE event is counted if the elemental status satisfies the maximum tensile strain criterion or the Mohr–Coulomb criterion, and each AE event will be orderly recorded and counted for every loading step. The rock macroscopic damage using cumulative AE counts was proposed (Tang et al. 1997) referring to Eq. (2):

$$D_s = \frac{N}{N_0}, \tag{3}$$

where N represents the accumulated AE counts obtained at a certain loading step before sample failure, and the parameter N_0 represents the total accumulated AE count when the sample fails.

2.3 Simulation Details

The size of the numerical model is designed with reference to the uniaxial compression test, whose cylindrical length and diameter are 100 mm and 50 mm, respectively. The simulation of the low-amplitude wave propagation through damaged rock is divided into two loading stages, i.e., static loading stage and dynamic loading state. At the first loading stage, static load is conducted with the external displacement of 0.002 mm and applied to the specimen step by step in the axial direction. The different damage degrees of the rock can be captured in any loading step, and the damage degree is quantified by Eq. (3). At the second loading stage, dynamic load is applied on one side of model along the axial direction. A half-sine pulse wave is employed in the analysis of wave attenuation and heterogeneity effects. Other types of waveforms, i.e., rectangular wave and exponential decay wave, are adopted to study the dependence of wave propagation and attenuation on waveforms. It should be noted that the amplitude of the pulse wave must be sufficiently low to avoid damage generation and AE events during the wave propagation. The viscoelastic nonreflecting boundary is applied to the other three boundaries to eliminate the reflected wave at boundaries.

Moreover, dynamic loading tests were performed in advance to determine the mesh ratio (ratio of mesh size to wavelength) and, thus, improve the calculation efficiency without losing accuracy. The ratio of the simulated to theoretical wave velocities (one-dimensional wave velocity in a homogeneous material) is used as the criterion to determine the mesh ratio. Figure 1 shows the dependence of the ratio of the simulated to theoretical wave velocities on the mesh ratio. It was found that the velocity ratio is close to 1 when the mesh ratio of the mesh is smaller than 0.02. Therefore, a mesh ratio of 0.02 is used in the numerical simulation in this paper.

2.4 DIP-Based Model Setting

DIP is a method of converting image information into digital signals and storing them in computers. Some imperceptible but important image information then could be obtained by mathematical algorithms. DIP techniques have been used widely in recent years to detect discontinuity geometry (Hadjigeorgiou et al. 2003), to analyze rock failure process (Zhu et al. 2006), and to predict rock failure (Itoh et al. 1996). DIP techniques are employed in this study to build a mesostructured model and characterize rock heterogeneity.

DIP technique Digital images are represented by a finite number of numerical pixels. The color information of true color digital images, such as location and intensity, is discrete when compared to the rectangular array of pixels. The location of each pixel usually is determined by cross lines in a coordinate system, and the color generally is described by color space, such as RGB space or HSI space (Gonzalez 1997). The RGB color space is established by three primary

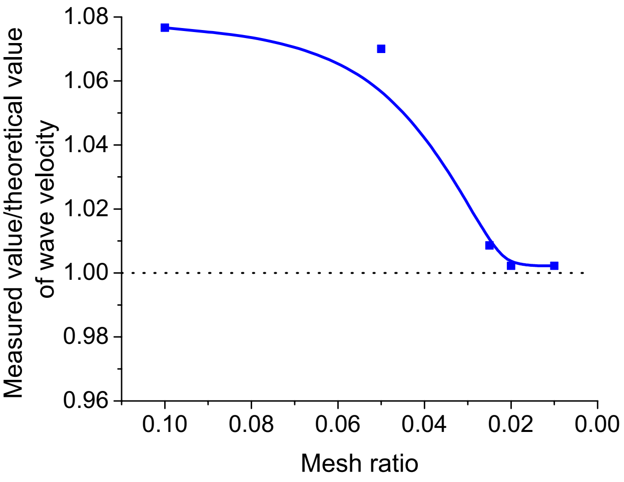

Fig. 1 The ratio of simulated to theoretical wave velocities vs. the mesh ratio

colors, i.e., red, green and blue, and each pixel has three integer variables ranging from 0 to 255 in terms of those three primary colors (Yue et al. 2003). Based on how humans perceive colors, the HSI space is an alternative to the true color space (Smith 1978). The hue component H means the dominant wavelength of the color stimulus, whose value is from 0 to 360. The saturation component S denotes the bright-colored degree of color, ranging from 0 to 1. The intensity component I (from 0 to 1) refers to the color's lightness. This color space could express human visual perception more directly. As a special case, the gray digital image represents that each pixel is only one sample color, and the gray level range is from 0 (black) to 255 (white) in an imitation of the RGB color space.

The mesoscopic structure of the surface or internal characteristics of rock samples could be observed by macroscopic observation, photograph, or CT scanning technology. The color information of each pixel could be distinguished according to the discrete color space when the mesoscopic structure is recorded by digital images. The numerically similar pixels in the color space could be identified as one material, which may be one type of mineral or a cluster of voids (Zhu et al. 2006). The color thresholds are set to distinguish one group of pixels from another. Each group can be specified with particular material properties, such as elastic modulus or compressive strength. Consequently, the material property could correspond to every pixel to reflect the mesoscopic characteristic of the rock material.

Numerical model In this paper, gray digital images retrieved from Hunan granite (HNG), Shandong granite (SDG), Shandong sandstone (SDS) and Inner Mongolia basalt (IMB) specimens by X-ray CT scanner are incorporated into RFPA. Note that an X-ray Micro-CT XRM 500 scanner was used. It has a 160-kV X-ray light source with an exposure time of 18 s. The maximum scanning range is 100×100 mm, and the corresponding pixel of its charge coupled device is 2000×2000, which satisfy the requirement of model establishment. The gray level of a pixel in the CT image is dependent on the density. Due to the small difference among the mineral densities and the influence of image noise, the gray histogram of the sample generally shows a single-peak feature as shown in Fig. 2, which is not conducive to determine the gray thresholds (Qajar and Arns 2016).

To precisely determine the gray thresholds, another method of Chen et al. (2004) and Zhu et al. (2007) was utilized. Taken the HNG as an example, the specific process of such method is briefly introduced herein. As shown in Fig. 3, where HNG meso-structure model is established, the resolution of the digital image in Fig. 3a is 300×600 pixels, and each pixel is considered one element. It retains the original heterogeneous information of the HNG. The main minerals in HNG are quartz, feldspar and mica, and their distributions in CT images are shown in Fig. 3a. The differences in the grayscale of different minerals are small but visible to the naked eye. A horizontal line containing those three minerals is selected as the scanning line and the gray level corresponding to each pixel on this line could be obtained, as shown in Fig. 3b. The peak/valley of the curve in Fig. 3b corresponds to the position of the mineral on the scanning line, and the abrupt change of curve corresponds to the boundary of the mineral. The density of the mica (3.12 g/cm^3) is significantly larger than that of quartz (2.65 g/cm^3) and feldspar (2.57 g/cm^3). Therefore, in Fig. 3b, the three peaks with the gray level of around 181–200 indicate the position of the mica on the scanning line. To highlight the mica as much as possible, we set 181 as the gray threshold, and the pixels with gray values greater than 181 are identified as mica. Most of the valleys in Fig. 3b indicate the location of feldspar as it has the smallest density. As shown in Fig. 3b, a gray threshold line with a value of 151 could well distinguish the valleys representing feldspar from the peaks representing quartz.

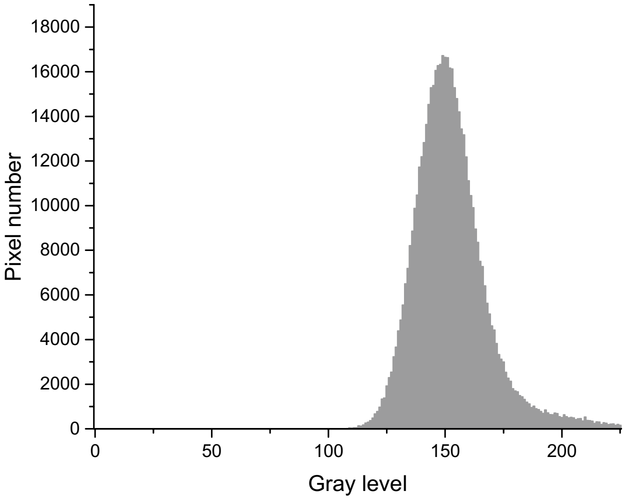

Fig. 2 Gray histogram of digital image of HNG

The segmented result of HNG is presented in Fig. 3c. The mechanical parameters of three minerals are listed in Table 1 (Bass 1995; Fei 1995; Ichikawa et al. 2001). The model establishment of the other three samples (shown as Fig. 4) is similar to that of the HNG. The minerals examined in SDG are the same as those in HNG. Combined with specific CT image, the gray thresholds used in the SDG model are 116 and 150. Sandstone is mainly composed of quartz, feldspar and a small amount of clay minerals. Herein, we take chlorite as the representative of clay minerals, and its input parameters are listed in Table 1 (Zhou et al. 2011). And the gray thresholds of SDS are 86 and 100. The effect of the primary pores in the basalt (IMB) on the mechanical properties of the sample is significant. Therefore, the pixels with grayscale less than 60 are identified as pores,

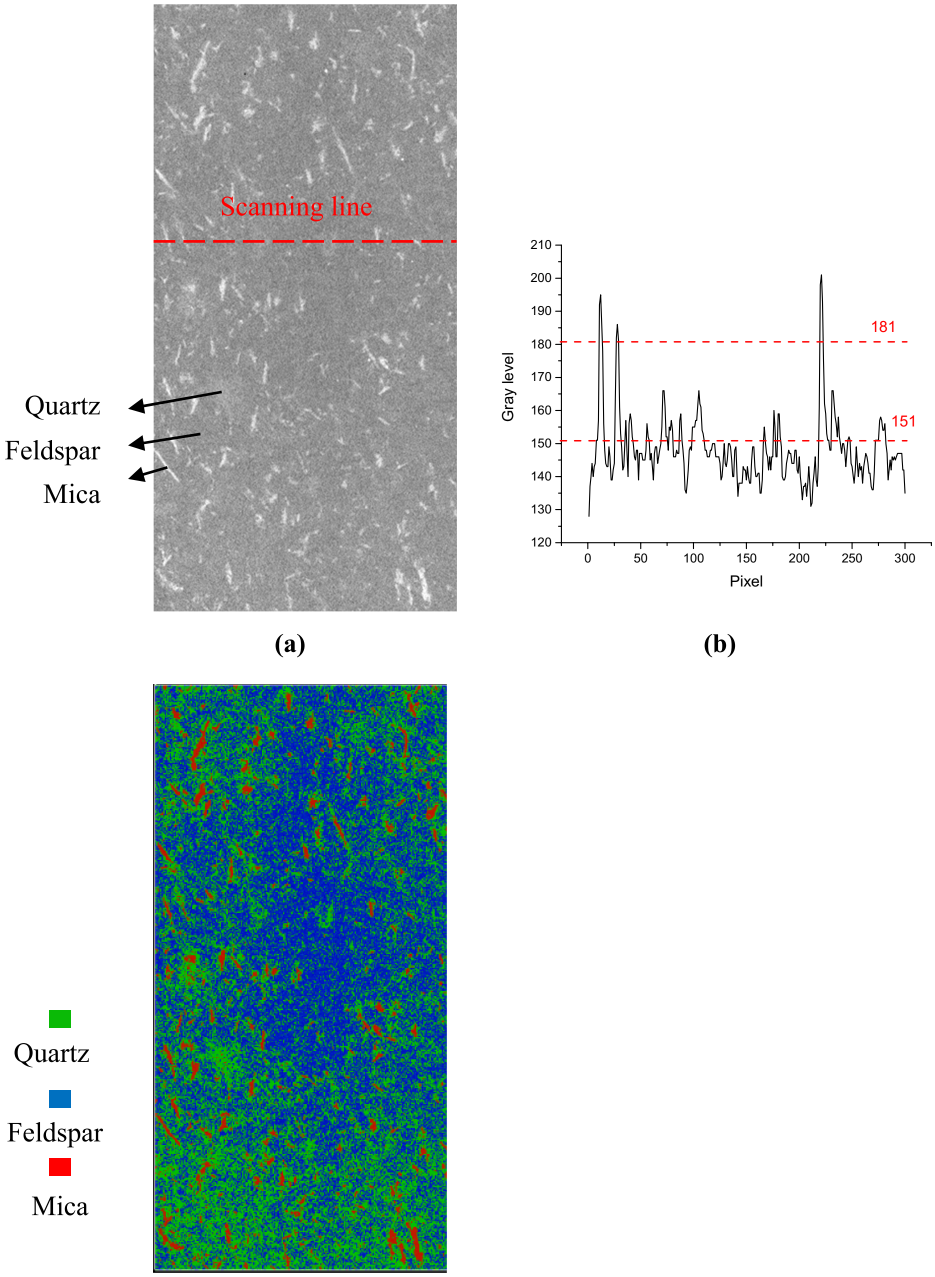

(a) (b)

(c)

Fig. 3 Establishment of HNG meso-structure model: **a** reconstructed digital images after CT scanning and the scanning line; **b** the distribution of gray level on the scanning line; **c** the segmented result for meso-structured characterization

Table 1 Mechanical parameters of minerals

Mineral type	Young's modulus (GPa)	Uniaxial compressive strength (MPa)	Uniaxial tensile strength (MPa)	Poisson's ratio	Internal friction angle (°)	Density (g/cm^3)
Quartz	96	700	47	0.08	38	2.65
Feldspar	67	400	33	0.27	35	2.57
Mica	40	250	25	0.25	30	3.12
Chlorite	19	53	5	0.38	21	3.30

Fig. 4 The CT-scan images of rock samples, the segmentation results and the corresponding gray thresholds: **a** SDG; **b** SDS; **c** IMB

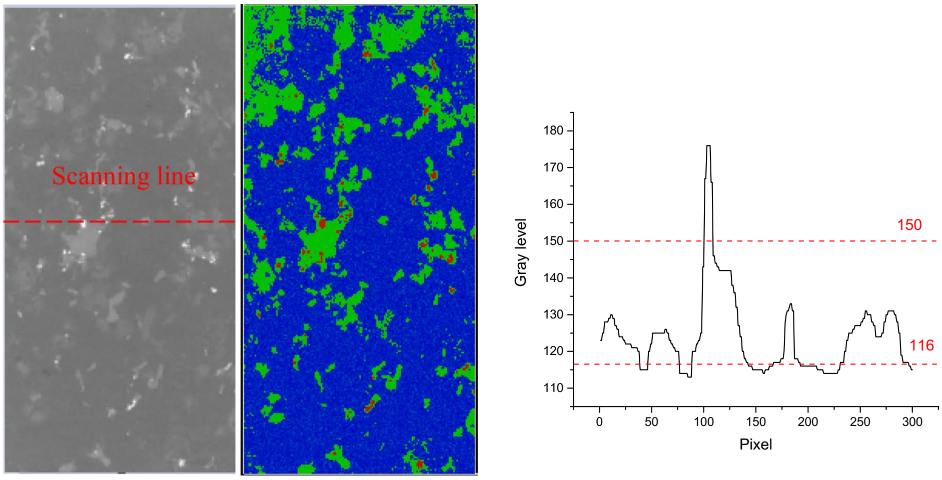

(a) SDG

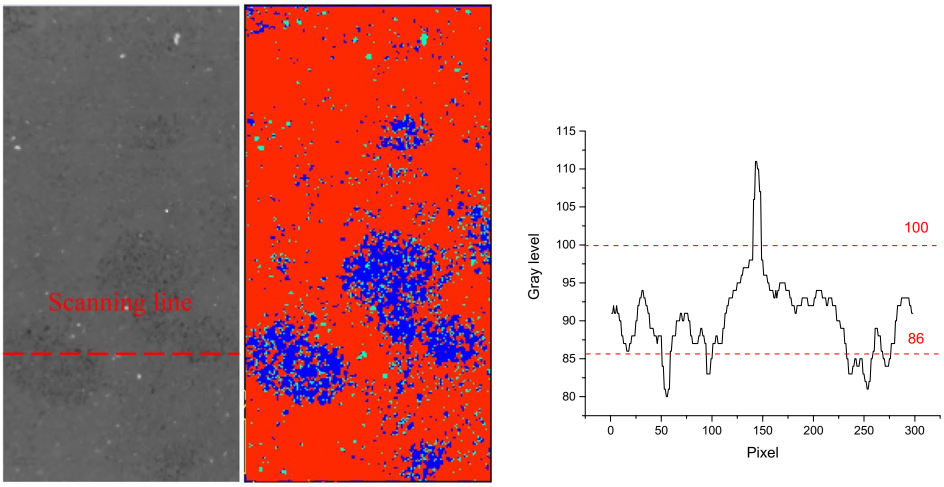

(b) SDS

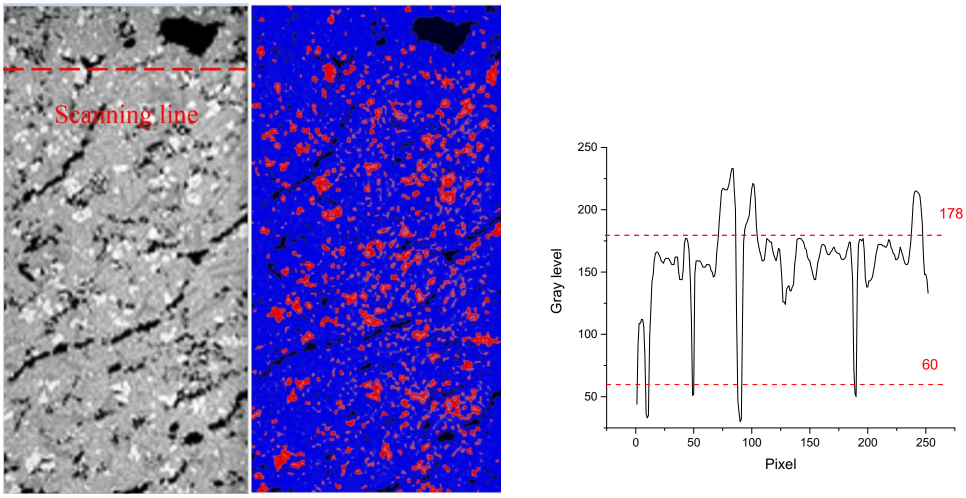

(c) IMB

and the gray threshold of 178 is used to divide the two main minerals in the solid phase, namely quartz and feldspar. It is worth noting that the amendment of input parameters through attempts is necessary when considering the fuzzy treatment of the grid boundary and the limitations of the two-dimensional model.

3 Verification

To calibrate the numerical model, we experimentally investigated damage evolution of HNG under static uniaxial compression and its effect on P-wave propagation during loading process. During testing, the stress–strain evolution, AE behaviors and low-amplitude wave propagation in HNG samples were monitored, as shown in Fig. 5. The compression test was performed on an MTS 647 machine with a displacement control mode of 0.075 mm/s. AE behaviors during loading process were continuously recorded using the PCI-2 AE system with its acquisition rate and threshold trigger value setting at 1.0 MHz and 40 dB, respectively. Low-amplitude P-wave propagation in HNG sample along the loading direction was monitored using an Olympus 5077PR ultrasonic system.

To assess the effect of damage on low-amplitude wave propagation, the HNG samples were first loaded to constant stress values with respect to UCS of the HNG. The samples were unloaded when the axial stress reached the setting values. During loading, low-amplitude wave propagation in HNG along axial direction was recorded at the setting stress levels. AE behaviors were continuously detected during the entire compression process. Meanwhile, low-amplitude wave propagation in HNG before and after loading was also measured to evaluate the influences of loading-induced damage on wave propagation in HNG samples. Notably, the loading-induced damage in the HNG samples during physical tests is also defined as the ratio of the accumulated AE counts in the process of loading divided by the total accumulated AE counts during the entire loading period (Ohtsu and Watanabe 2001), which can be determined by the Eq. (3).

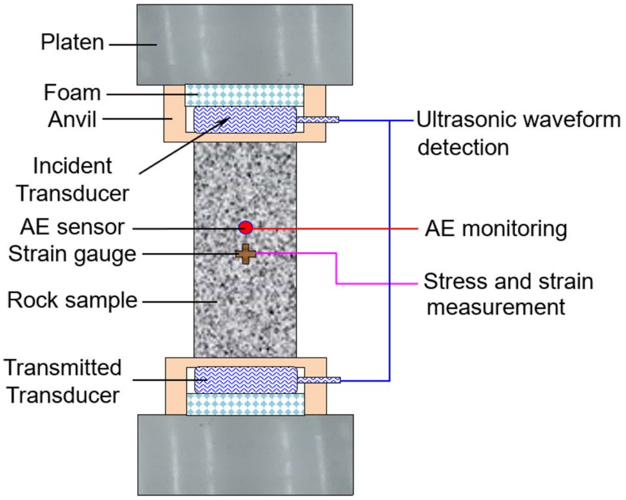

Fig. 5 Diagram of the experimental setup for P-wave propagation measurement and AE detection during uniaxial compression

To verify the correctness of the simulation method, we established a numerical model in RFPA after CT scanning of HNG and reconstruction of internal structure of sample by DIP technique. The ultimate failure modes and stress–strain curves from laboratory tests and numerical simulations are shown in Figs. 6 and 7, respectively.

The ultimate failure mode in numerical simulation is similar to that from the laboratory test and shows obvious shear failure characteristics. The angle between the normal direction of rupture surface and the longitudinal axis of the sample in numerical simulation is approximately 70°, which is slightly less than that in the laboratory test, i.e., 80° approximately. The difference may be due to the two-dimensional limitations of the numerical model.

As shown in Fig. 7, the elastic modulus from numerical simulation agrees well with that obtained from laboratory test. The brittleness of the numerical rock sample is also demonstrated through the rapid stress drop of stress during failure. The nonlinearity of the stress–strain curve at the initial stage of laboratory test, which is attributed to the closure of voids and microcracks, could not be captured by the constitutive model in RFPA. There is also a minor difference in the magnitudes of the peak stress obtained from laboratory test and numerical simulation. We believe those differences are because of the limitations of the 2D numerical model. The complexity of cracks in three-dimensional solids (Zhou et al. 2019, 2020) cannot be fully described by the numerical model built from a single CT slice.

We also studied the dependence of wave amplitude on rock damage with the numerical simulation and laboratory tests. Figure 8 shows the P-wave amplitude variation (the ratio of amplitudes of transmitted wave through damaged rock to intact rock) for HNG from laboratory test and numerical simulation. In general, the numerical results are in good agreement with the experimental ones. The amplitude of the P-wave decreases as the damage increases, and it rapidly drops when the damage is high in both simulation and testing results. When the damage degree is low, the relatively lower wave amplitude from numerical modeling with contrast to laboratory measurements may be caused by the compaction of the rock. This process cannot be reproduced in RFPA. When the damage degree is 0.4, the P-wave amplitude variation obtained from the laboratory test is smaller than that obtained from the numerical modelling. One probable reason is the limitation of 2D numerical model. Meso- or macro-cracks have been induced in the samples when $D = 0.4$ and the geometry of these cracks is more intricate in the real 3D materials. Thus, the amplitude attenuation obtained by experiments is greater than that obtained by 2D numerical modelling. Another possible reason is the accuracy of the test data at the high-damage stage. In fact, the failure of the samples

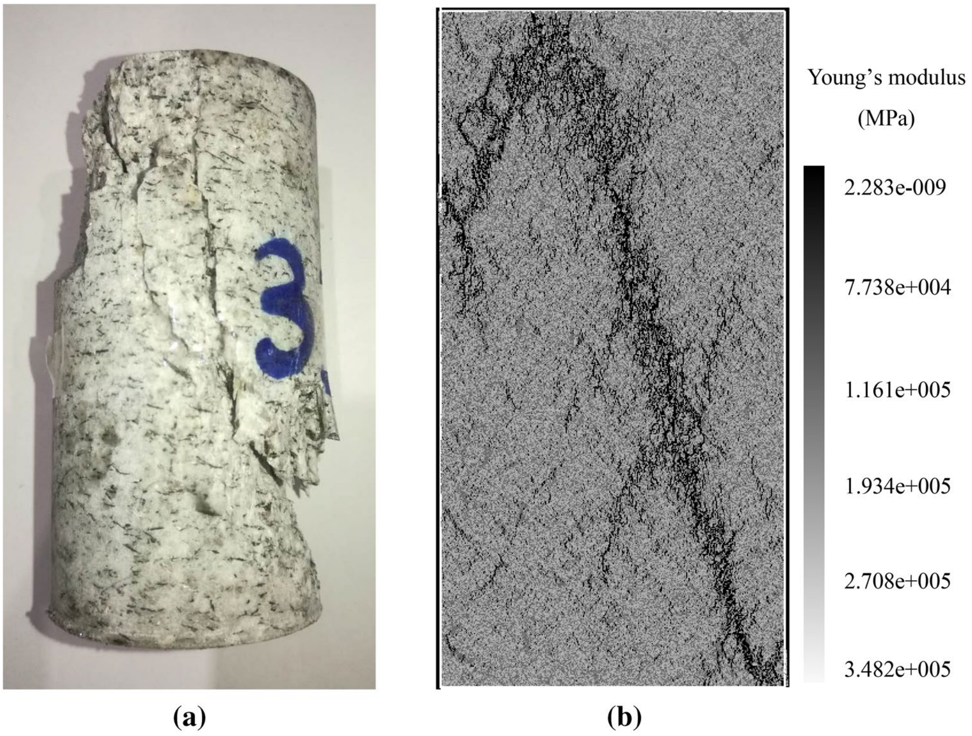

(a) (b)

Fig. 6 The ultimate failure modes for HNG under uniaxial compressive loading from: **a** laboratory test; and **b** numerical simulation (the Young's modulus contour)

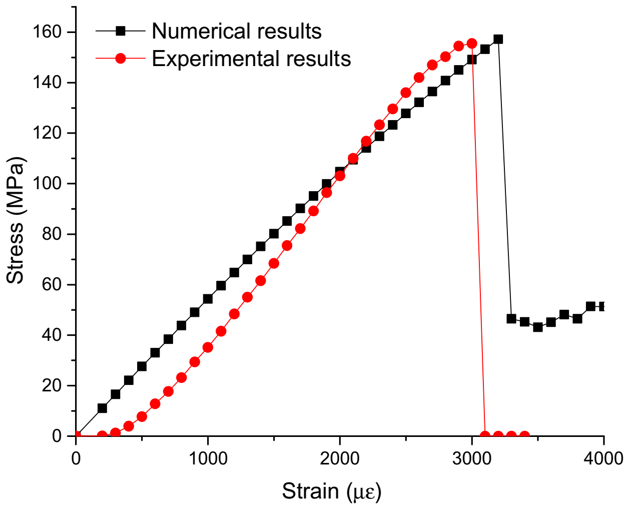

Fig. 7 Stress–strain curve for HNG under uniaxial compressive loading from laboratory test and numerical simulation

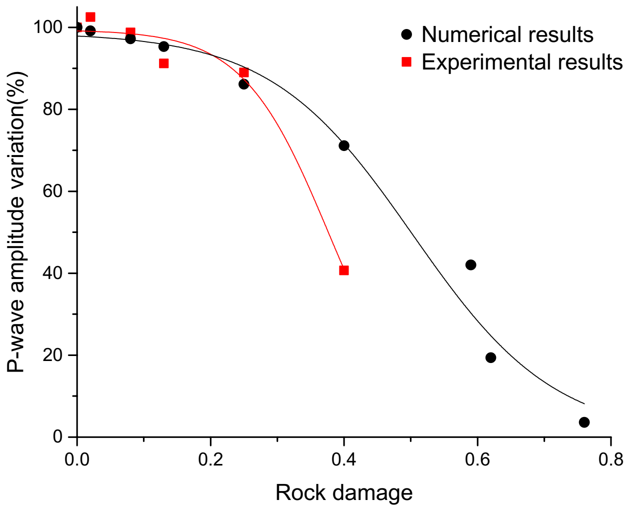

Fig. 8 P-wave amplitude variation (the ratio of amplitudes in damaged rock to intact rock) for HNG from laboratory test and numerical simulation

when approaching the ultimate compressive strength is instantaneous, and the data of rock damage of 0.4 and above are insufficient. This is also why the experimental results for the damage of 0.4 or higher are not presented in Fig. 8. However, the effective value of damage in simulation can reach approximately 0.8 through finer loading control, which is an advantage of numerical simulation over laboratory test.

4 Wave Propagation in Different Types of Damaged Rocks

In this section, the numerical models of HNG, SDG, SDS and IMB samples were employed to investigate wave attenuation in rock. A half-sine pulse wave was applied to the numerical models of different damage degrees, which were achieved by loading the samples at different stress levels in static compression tests. The wave signal after propagating 95 mm in the sample (100 mm long) was recorded, and the amplitude and arrival time of the first wave signal were employed to analyze the wave attenuation and slowness, respectively.

The wave attenuation ratio is used to describe the wave attenuation, which is defined as

$$\frac{A_\mathrm{i} - A_\mathrm{D}}{A_\mathrm{i}} \times 100\%, \tag{4}$$

where A_i and A_D are the measured amplitude at the same point in the intact rock and the damaged rock, respectively. Figure 9 shows the relationship between wave attenuation ratio and the damage of different rocks.

The amplitude attenuation ratio and its increasing rate both increase with increasing damage, regardless of rock types, which is coincident with laboratory observations (Jaeger et al. 2007). With increasing loading or damage, the microstructure and micro-pores were crushed in the initial loading stage followed by the generation of local cracks and the major fracture. The effect of large-scale local cracks on amplitude attenuation is much greater than that of microstructures for the low-amplitude stress wave (Goodman 1980). Therefore, with increasing damage, the generation of large-scale cracks and fractures leads to the sharp increase in attenuation ratio and the upward concave exponential curve of attenuation ratio vs damage, as shown in Fig. 9.

The dependence of wave attenuation ratio on damage follows exponential function in a form of

$$a \times (\exp(b \times D_\mathrm{s}) - 1), \tag{5}$$

where constants a, b and the correlation coefficients R^2 for four types of rocks were determined after best fitting and are listed in Table 2. The constant a reflects the magnitude. As seen in Table 2, the SDG has the greatest value of a, i.e., 201.1; while the value of a (3.01) for IMB is the smallest. The constant b describes the concaving degree of the fitting curve and a large value of b indicates a more concave curve, and vice versa. As seen in Table 2, the value of b (4.10) for SDS and IMB is the greatest, while SDG's b value is the smallest. The difference among the values of a and b for those four types of rocks could be explained by the different features of pre-existing damage and damage evolution during loading of those rocks.

Figures 10 and 11 present the evolutions of damage and AE counts of different rocks during the whole uniaxial compressive loading process, respectively. In Fig. 10, D_s was calculated by Eq. (3) under different stress levels. And the black cells in Fig. 10 indicate the defects whose mechanical strength is a nonzero infinitesimal and set to 1e−9 MPa. As observed in Fig. 10, with increasing loading, the microstructure and micro-pores were crushed in the initial loading stage followed by generation of local cracks, which were subsequently interconnected to form a major fracture eventually resulting in the sample failure. The same evolutionary process is also reflected in the changes in the AE counts. As shown in Fig. 11, the red bar indicates the AE counts in each calculation step. At the low stress stage, the number of AE events was small, indicating very few damages were generated except for several jump points. Those jump points reflect the form of local cracks. When the sample approached failure, a great number of AE events appeared, meaning catastrophic failure of the sample. Meanwhile, the damage increases steadily until the samples are close to failure and it grows sharply.

In Eq. (5), the constant a describes the magnitude of the attenuation of the wave amplitude, which is mainly determined by the proportion of damage from cracks. In our simulation results, this is obvious during the initial loading phase. As shown in Fig. 10, when the damage value is low, the number of cracks generated in the SDG and HNG models is much larger than that in the SDS and IMB models.

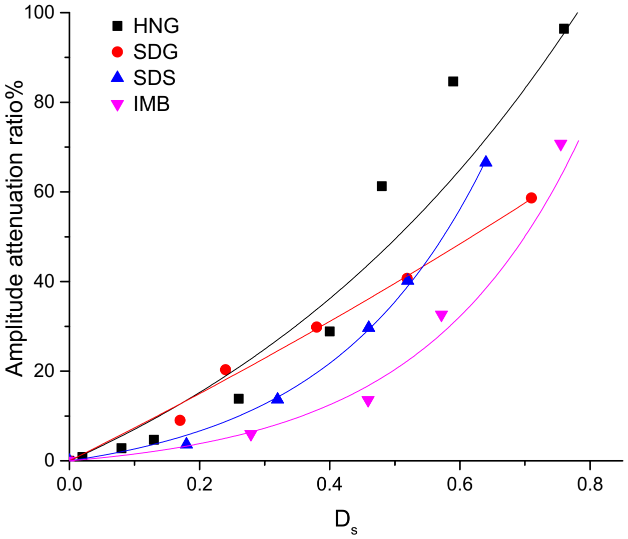

Fig. 9 Wave attenuation ratio as a function of damage in HNG, SDG, SDS and IMB

Table 2 Constants and correlation coefficients for four types of rocks after best fitting

Fitting equation $a \times (\exp(b \times D_\mathrm{s}) - 1)$	HNG	SDG	SDS	IMB
a	40.9	201.1	5.23	3.01
b	1.58	0.35	4.10	4.10
R^2	0.97	0.99	0.98	0.98

Fig. 10 Damage evolution of different rock models during the whole compressive loading process (the maximum principal stress contour): **a** HNG; **b** SDG; **c** SDS; and **d** IMB and the circle, oval and dotted line refer to the micro-defects, meso-defects and macro-defects, respectively

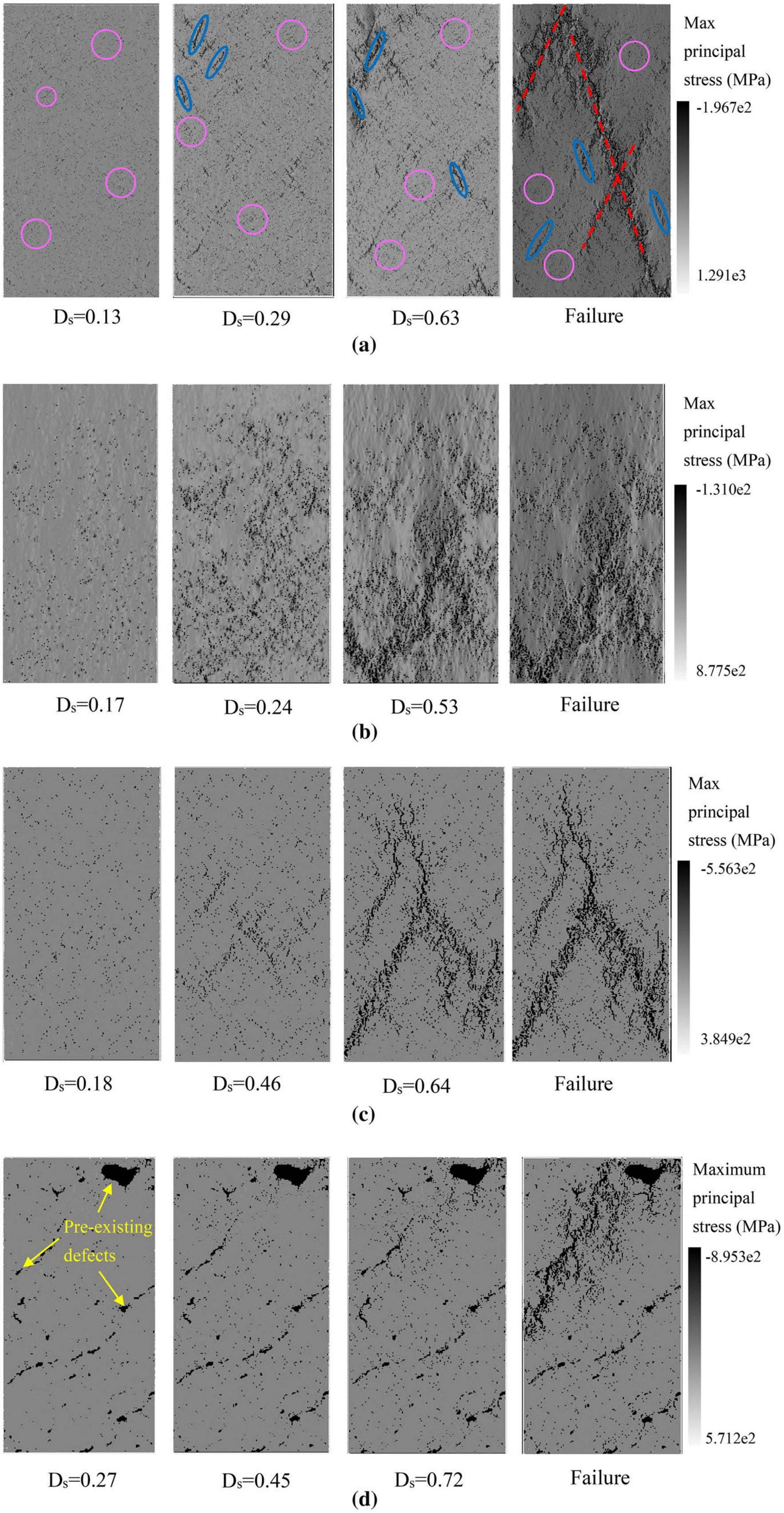

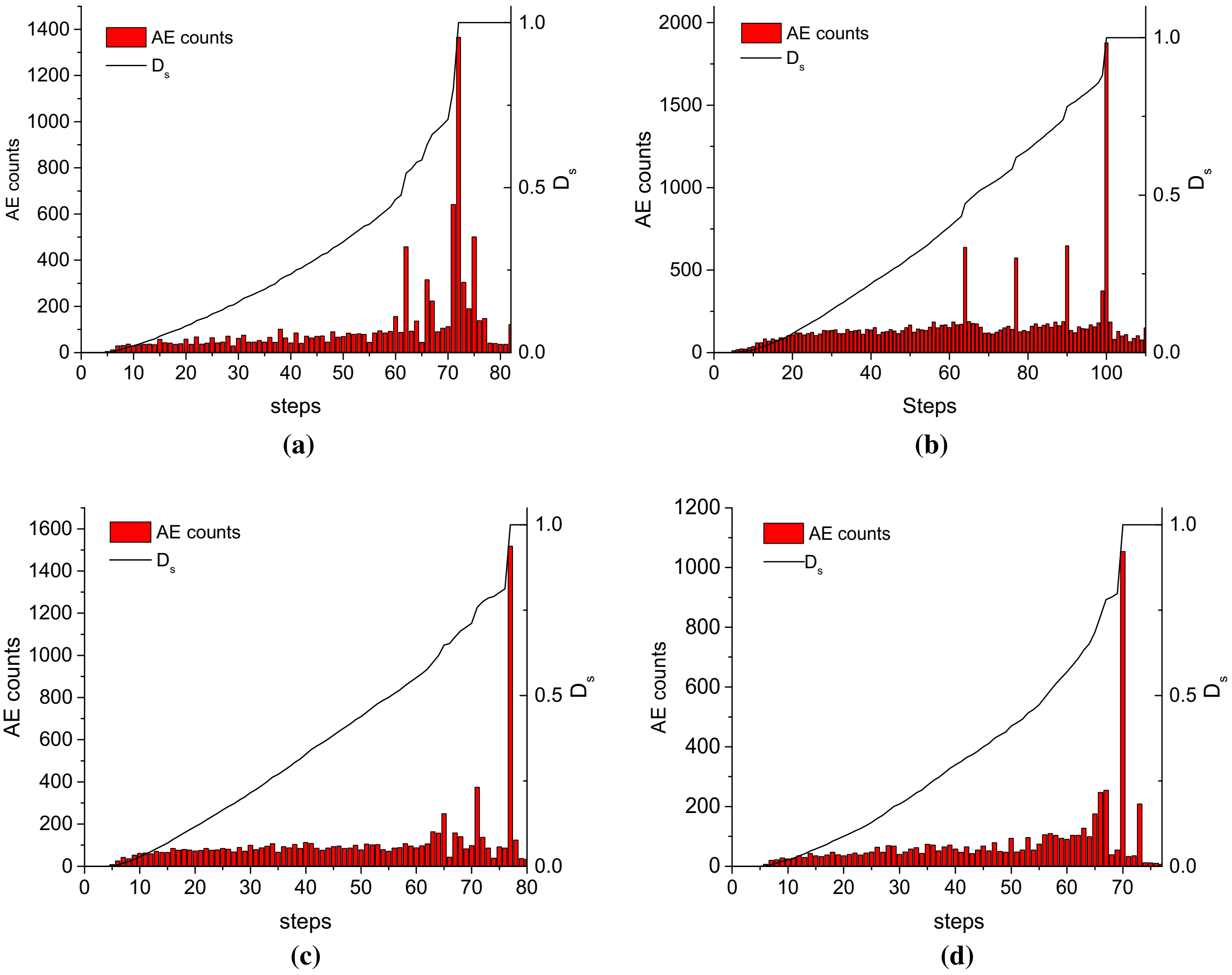

Fig. 11 The evolution of AE counts during whole loading process: **a** HNG; **b** SDG; **c** SDS; and **d** IMB

Therefore, the amplitude attenuation ratio of SDG and HNG models is greater than that in SDS and IMB models. This is due to the large differences in mechanical properties between the minerals in the granite. Minerals with lower compressive strength first fail under external load, forming micro-pores. These defects are further expanded under concentrated stress to form cracks that have an effect on wave amplitude attenuation (Fig. 10a, b). However, in the relatively homogeneous SDS and IMB models, the initial damage of the rock is dominated by micro-pores at the initial stage of loading (Fig. 10c, d). Hence, the amplitude attenuation ratio of this stage is lower than that of the first two models, that is, the constant *a* is small.

As the external load increases, the formation of macroscopic cracks in the model leads to a rapid increase in the amplitude attenuation ratio. The rate of increase can be represented by the constant *b* in Eq. (5). The larger the value of *b*, the greater the impact of damage on the attenuation of the amplitude as the damage increases, that is, the proportion of macroscopic cracks increases. The statistics of acoustic emission in Fig. 11 indicate the difference in constant *b*. For the SDG model with the smallest *b* value (0.35), there are three obvious jump points in the cumulative number of AEs during the whole loading process (Fig. 11b). However, the AE counts of the other three models, i.e., HNG model, SDS model and IMB model, shows continuous growth until a sharp increase at failure. At the same time, through comparing the AE evolution process of the four models, we can find that the smoother the increase of AE counts before failure, the larger the *b* value.

To describe the decay of wave velocity, the wave slowness ratio is proposed:

$$\frac{V_i - V_{\mathrm{D}}}{V_i} \times 100\%, \tag{6}$$

where V_i and V_D are the velocities in intact and damaged rocks, respectively. Figure 12 shows the dependence of wave slowness ratio on damage for HNG, SDG, SDS and IMB. It could be seen that the wave slowness ratio increases as the rock damage increases. The wave slowness is the highest for low-amplitude wave propagation in HNG, which is the same as the wave attenuation shown in Fig. 9. However, the distinction among four curves in Fig. 12 is smaller than that in Fig. 9, indicating that wave velocity is less sensitive to rock damage compared with wave amplitude.

5 Propagation of waves of different waveforms in damaged rocks

In nature, the wave might be of different forms, e.g., half-sine wave, rectangular wave and exponential decay wave (Li 2014). In this study, we investigated low-amplitude half-sine, rectangular and exponential decay wave propagation in damaged rock, whose waveforms follow the Eqs. (7), (8) and (9), respectively:

$$\sigma(t) = \begin{cases} \sigma \sin(\omega t), & t \in (0, \pi/\omega) \\ 0, & \text{others} \end{cases} \tag{7}$$

$$\sigma(t) = \begin{cases} \sigma, & 0 \le t \le \tau \\ 0, & \text{others} \end{cases} \tag{8}$$

$$\sigma(t) = \begin{cases} 0, & t < 0 \\ \sigma \exp(-\lambda t), & t \ge 0 \end{cases}, \tag{9}$$

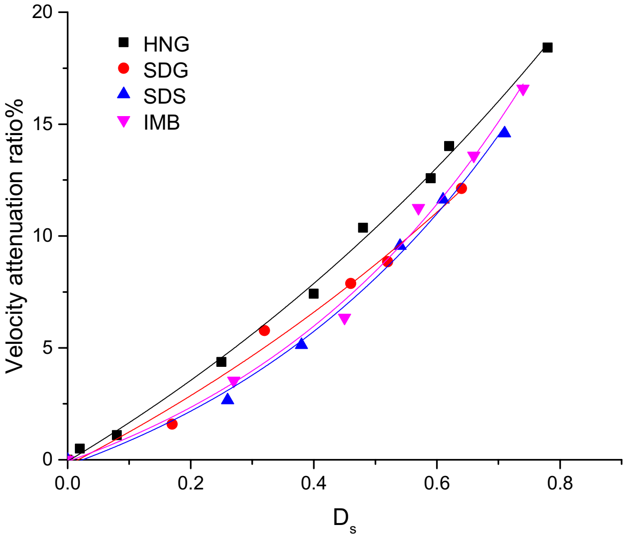

Fig. 12 Velocity slowness ratio vs damage for HNG, SDG, SDS and IMB

where ω is angular frequency and λ is a time constant. In above equations, σ is set to 10 MPa to ensure that there is no induced damage during the stress wave loading phase. We set the angular frequency of the half-sine wave as 30π kHz, and τ in Eq. (8) equals 33 μs, to ensure that the duration of wave is consistent. For exponential decay waves, assuming that the duration of the pulse wave ends as its amplitude decreases from σ to 1e−8 Pa, the parameter λ can be calculated as 4.7e5. The model size is 50*100 mm and consists of 150 × 300 cells, whose homogeneity index, m, equals to 3.

Figures 13 and 14 show the wave attenuation ratio and wave slowness ratio vs rock damage, respectively, where the incident waves include half-sine wave, rectangular wave and

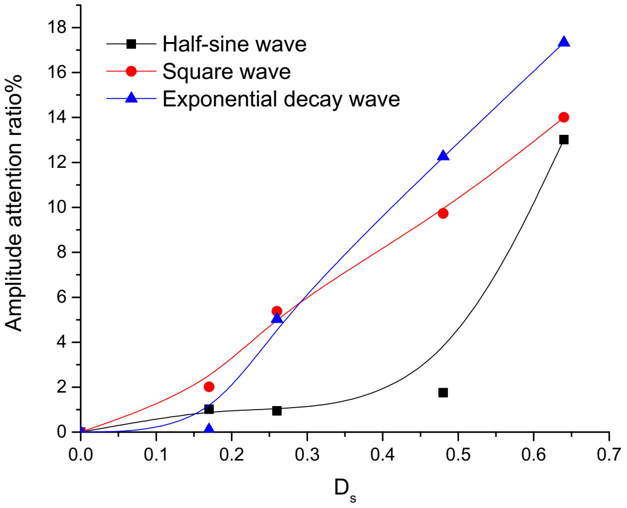

Fig. 13 Wave attenuation ratio vs damage for half-sine, rectangular and exponential decay wave propagation in damaged rock

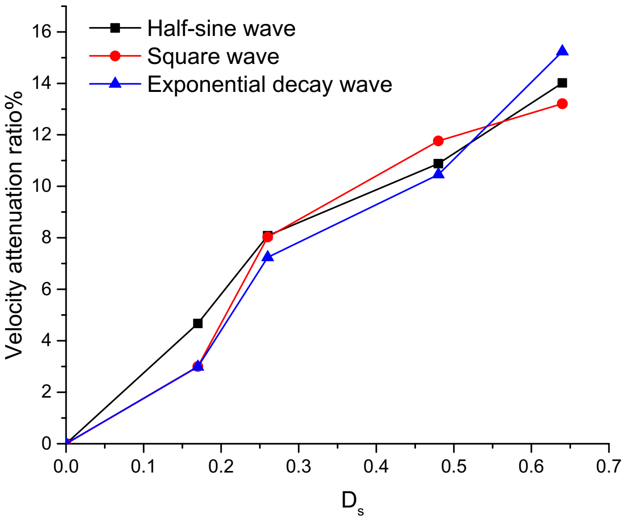

Fig. 14 Velocity slowness ratio vs damage for half-sine, rectangular and exponential decay wave propagation in damaged rock

exponential decay wave. It was found that the wave attenuation ratio increases, i.e., the wave amplitude decreases, with increasing damage regardless of waveforms. When the damage is low, $D_s < 0.3$, square wave attenuation ratio is the largest; while the damage is higher, exponential decay wave attenuation ratio is the largest. The waveforms have very few effects on the wave velocity in damaged rocks, as shown in Fig. 14.

6 Rock Quality Evaluation and Classification Scheme for Rock Fracturing Degree

Wave propagation features could be adopted to evaluate rock quality, as defects in rock could affect wave properties, e.g., velocity and amplitude. Wave velocity has been widely used to assess rock quality. Using P-wave velocities, Fourmaintraux (1976) introduced a quality index IQ_V of the rock:

$$IQ_V\% = \frac{V_{P,meas}}{V_{P,theor}} \times 100\%, \tag{10}$$

where $V_{P,meas}$ is the measured P-waves velocity in rock, and $V_{P,theor}$ is the P-wave velocity in an "intact" rock without cracks and pores.

In this paper, it is confirmed that compared with wave velocity, wave amplitude is more sensitive to rock damage/rock porosity. Therefore, an updated rock quality index using wave amplitude was proposed,

$$IQ_A\% = \frac{A_D}{A_I} \times 100\%, \tag{11}$$

where IQ_A is quality index defined by wave amplitude, A_D is the amplitude of transmitted wave through the damaged rock, and A_I is the amplitude of transmitted wave through the "intact" rock. The results of the updated quality index, IQ_A, versus the damage of different samples are shown in Fig. 15a.

The defects at different scales in rock sample could be reflected by rock damage. For rock samples with the same porosity or damage, those with larger-scale defects, e.g., joints, could more significantly influence wave propagation, e.g., more wave velocity slowness and more wave amplitude attenuation (Goodman 1980). Therefore, according to the dominant scale of defects in rock, the state of rock damage was divided into three types, i.e., the micro-defect dominant damage, the meso-defect dominant damage, and the macro-defect dominant damage. And we classified and linearly fitted the scattered data and obtained the relationship between IQ_A and D_s for those three conditions, as shown as Fig. 15b.

For the micro-defect condition, the relationship between IQ_A and D_s be expressed as:

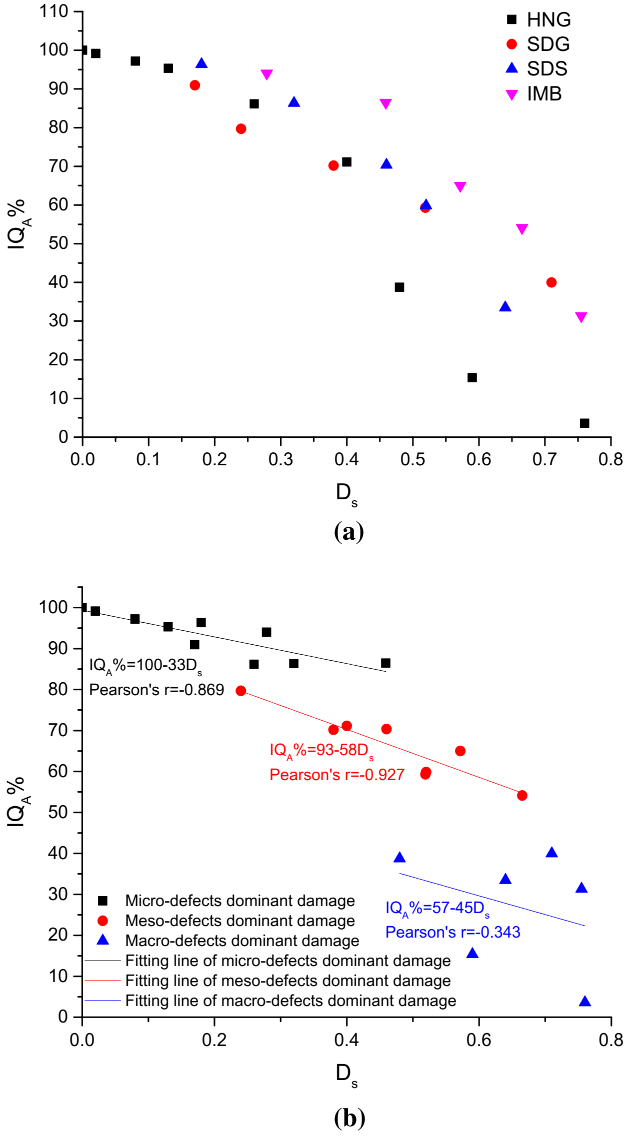

(a)

(b)

Fig. 15 The quality index versus rock damage: **a** the quality index versus damage of HNG, SDG, SDS and IMB at different loading levels; and **b** the quality index versus damage dominated by different scales of defects

$$IQ_A\% = 100 - 33D_s. \tag{12}$$

The Pearson's coefficient is 0.869, showing a strong correlation.

For the meso-defect condition, the relationship between IQ_A and D_s could be expressed as:

$$IQ_A\% = 93 - 58D_s. \tag{13}$$

For the macro-defect condition, the relationship between IQ_A and D_s could be expressed as:

$$IQ_A\% = 57 - 45D_s. \tag{14}$$

To maintain consistency and to facilitate future applications, the linear fitting is still employed in the macro-defects stage, in spite of the small correlation coefficient (−0.343) probably due to the great difference of macroscopic fracture distributions in different rock samples.

According to the constitution of the micro-, meso- and macro-defects, the rock fracturing degree could be divided into three regions, namely slightly fractured region, moderately fractured region and strongly fractured region. Therefore, it is necessary to determine the critical lines of these three regions. To generalize the critical lines and for convenient application, the three fitting lines in Fig. 15b are unified in the following linear form:

$$\mathrm{IQ}_{\mathrm{Ai}} = \beta_{\mathrm{i}} - \alpha \times D_{\mathrm{si}}, \tag{15}$$

where i represents different defect scales, α and β are constants. α is the same for all three fitting lines to guarantee their parallelization, which could be determined by the average of the three fitting lines in Fig. 15b, i.e.,

$$\alpha = \frac{\sum_{i=1}^{3} \alpha_i}{3} = 45. \tag{16}$$

And then, the parameter β_{i} could be calculated by averaging the $\mathrm{IQ}_{\mathrm{Ai}}$ and D_{si} at different defect scales, i.e.,

$$\beta_{\mathrm{i}} = \mathrm{IQ}_{\mathrm{Ai}}(\mathrm{mean}) + \alpha \times D_{\mathrm{si}}(\mathrm{mean}). \tag{17}$$

For micro-defect condition, since the IQ_{A} must equal to 100% when the damage is zero, β should be 100 in micro-defects states. Thus, the critical line for slightly fractured region is

$$\mathrm{IQ}_{\mathrm{A}}\% = 100 - 45D_{\mathrm{s}}. \tag{18}$$

Similarly, the critical line for moderately fractured region is

$$\mathrm{IQ}_{\mathrm{A}}\% = 87.83 - 45D_{\mathrm{s}}. \tag{19}$$

And the critical line for strongly fractured region is

$$\mathrm{IQ}_{\mathrm{A}}\% = 56.59 - 45D_{\mathrm{s}}. \tag{20}$$

Therefore, the improved classification scheme for rock fracturing degree using wave amplitude attenuation and rock damage was established, as shown in Fig. 16.

In Fig. 16, the strongly fractured region means a great number of macro-scale discontinuities are formed; while, slightly fractured region indicates that the damage is mainly from micro-scale defects. For example, when the damage of HNG is 0.18, the corresponding IQ_{A} is 86%, and the defined point falls in Zone I in Fig. 16, indicating that the HNG is slightly fractured. When the damage of HNG increases to 0.26, and corresponding IQ_{A} decreases to 78%, the defined point falls in Zone II in Fig. 16. It means that the HNG has some large-scale defects and moderately fractured. And when the damage of HNG is 0.63 and corresponding IQ_{A} decreases to 30%, the defined point falls in Zone III in Fig. 16. The HNG is viewed as strongly fractured and close to failure. These are coincident with the observations in Fig. 10.

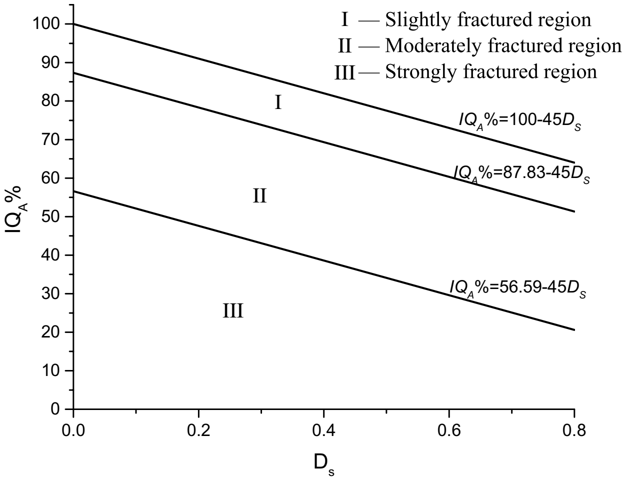

Fig. 16 An improved classification scheme for rock fracturing degree

7 Discussion

Findings in this paper show that damage has great effects on wave attenuation. The wave amplitude and wave velocity decrease as rock damage increases, and their relationships are shown in Figs. 9 and 12, respectively. However, there are two significant differences through comparison. First, at the same damage degree, the attenuation ratio of wave amplitude is approximately 5–10 times higher than that of wave velocity. Second, the effect of rock type on amplitude attenuation is stronger than that on wave velocity. The comparison shows that when evaluating rock damage (or rock quality), more accurate results will be obtained based on the wave amplitude parameters. Past experimental observations also proved this point, regardless of the rock damage caused by external loading (Suazo et al. 2016), heating (Chaki et al. 2008) or other means. This is mainly because amplitude is more sensitive than the others to rock damage (Watanabe and Sassa 1996; Deng et al. 2015; Zhu et al. 2016). Additionally, Svitek et al. (2017) claimed that the effect of rock anisotropy on wave velocity and amplitude is also different.

Figure 9 shows that wave attenuation ratio always increases with the increase of damage degree. However, its growth trend is different for different types of rocks. This might be caused by the heterogeneity of the rock. The homogeneity index m is assumed to be 2 for all numerical materials in the numerical modelling. The rock heterogeneity is affected by the particle size, distribution, and physical and mechanical properties of the numerical materials in the models among others (Zhu et al. 2006). Figure 17 illustrates the wave attenuation as functions of damage for rocks with different rock types (HNG, SDG, SDS and IMB) and different homogeneity indexes, where the influence of rock minerals is neglected and rock density, elastic modulus and compressive strength are set to be constant. The dependence of wave attenuation ratio on D_s is closer to linear with decreasing homogeneity index *m*. This finding further validates the results in Sect. 4. In the case of complex mineral composition and large differences in the properties and sizes of mineral grains, such as the SDG, the development of micro-cracks will be likely to be dominated by large-grain hard minerals, resulting in poor continuity of fractures. With increasing damage, the wave attenuation linearly grows. Nevertheless, the micro-cracks appear and join rapidly in the vicinity of the failure for more homogeneous rocks with simple mineral composition and small particle differences, e.g., SDS, forming a relatively penetrating fracture, and the wave attenuation vs damage follows a nonlinear exponential relation. Through comparing the curves of $m = 1.5$ and SDS in Fig. 17, it can be seen that it is insufficient to define rock heterogeneity only by homogeneity index *m*. Reconstructing rock meso-structures using DIP technique has obvious advantages in this regarding. In addition, although the differences in mineral properties and particle size in IMB are much larger than that in SDS, the growth trend of the amplitude decay ratio is similar. This may be because the evolution of cracks is affected by the primary porosity (Zhu et al. 2018). It indicates that more complex rock mass structures need to be considered in future study of the effects of rock heterogeneity on wave attenuation.

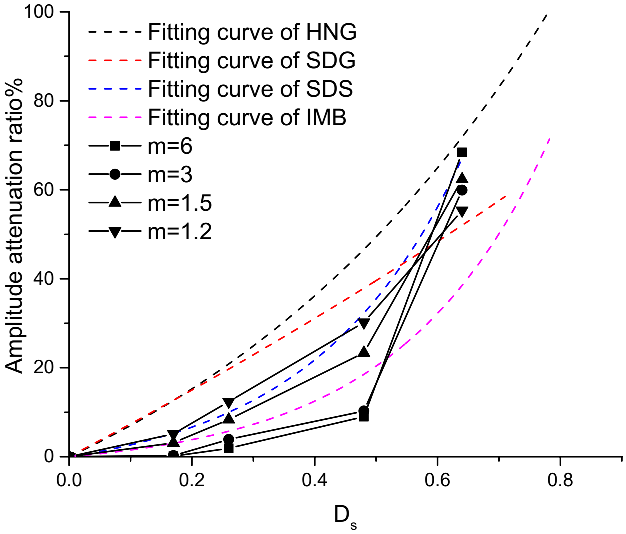

Fig. 17 Wave attenuation ratio as functions of damage for rocks with different homogeneity indexes and different rock types (HNG, SDG, SDS and IMB)

Considering that the propagation medium has the effect of selective absorption on sound waves (Müller et al. 2010), the wave features in the frequency domain could help us analyze the difference of attenuation among varied waveforms in the damaged rock mass. Through the fast Fourier transform, the frequency spectra for the incident wave and the transmitted waves in intact rock and damaged rock for half-sine wave, square wave and exponential decay wave (damage degree equals to 0.64) are shown in Fig. 18. In Fig. 18a, the amplitudes of high-frequency components of exponential decay wave and rectangular wave clearly are higher than half-sine wave. Therefore, due to the high-frequency filtering properties of rock materials (Müller et al. 2010), the exponential and rectangular waves attenuate more significantly. By comparing the spectra of the transmitted waves through the intact and damaged rocks (Fig. 18b, c), rock damage greatly enhances the rock high-frequency filtering function. The dominant frequencies of the half-sine, rectangular and exponential decay waves decreased by 25%, 34% and 26%, respectively, in damaged rocks when compared to intact rocks.

Figure 10a shows the defects of different scales in damaged rock (HNG), where the circle, oval and dotted line refer to the micro-defects, meso-defects and macro-defects, respectively. Notably, the state of rock damage could be divided into three types, i.e., micro-defects dominant damage, meso-defects dominant damage and macro-defects dominant damage, respectively. In addition, results in Fig. 15b demonstrated that the quality indexes of rocks are remarkably different for those three damage states even for the exactly same damage degree. For example, as shown in Fig. 15b, when the rock damage degree is about 0.48, the quality index of rock whose damage state is micro-defects dominated is as high as 86%. However, this value directly falls to about 70% and 38% when the rock damage is dominated by meso-defects and macro-defects although the damage degree is still equal to 0.48. Therefore, it could be suggested that for rock samples with same damage degree, those with larger-scale defects have more significant effect on rock quality, i.e., wave propagation.

Many efforts have previously been devoted to establishing a classification chart for rocks. From the perspective of porosity, Fourmaintraux (1976) established a chart of rock fissuring degree based on the decay of wave velocity. Differently, damage parameter directly can show the deterioration of rock properties, and wave amplitude is more sensitive to damage. Therefore, defining the quality index with wave amplitude is more accurate than that with velocity. However, there are many methods to define rock damage. Whether the damage defined by the other physical or mechanical parameters than that used in

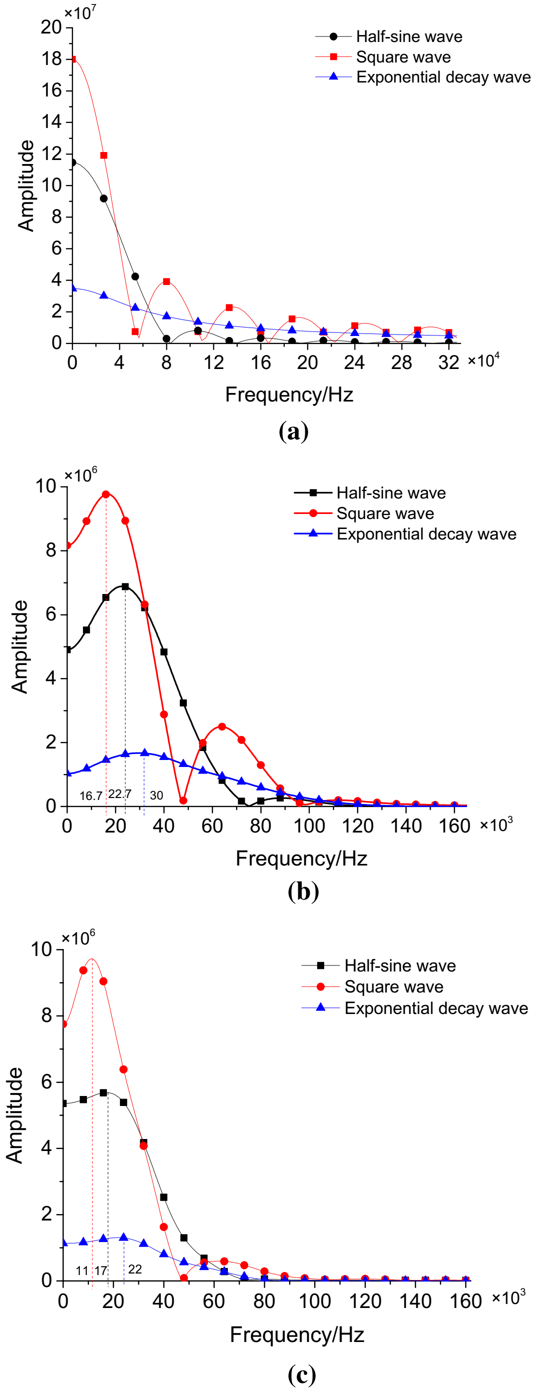

Fig. 18 Frequency spectra of: **a** incident wave; **b** transmitted wave through intact rock; and **c** transmitted wave through damaged rock

this paper is more suitable needs further study. In addition, the classification scheme for rock fracturing degree proposed in this paper requires further testing and field verifications.

8 Conclusions

Main conclusions of this paper are summarized as follows:

(1) Rock damage has a significant impact on the propagation of low-amplitude stress waves. Amplitude, wave velocity and dominant frequency all decrease as damage increases. Among them, the variation of amplitude is the most sensitive to rock damage.

(2) Rock heterogeneity affects the damage evolution in rock during loading, and hence, determines the amplitude attenuation characteristics. In the relatively homogeneous rock, the concentration of meso-scale discontinuities leads to a rapid increase of amplitude attenuation ratio when the damage is large. While in relatively heterogeneous rock, the rock damage is mainly from the generation of micro-scale cracks during loading, and the amplitude attenuation ratio increases linearly.

(3) The wave attenuation characteristics vary for wave signals with different waveforms in damaged rocks. Among half-sine wave, square wave and exponential decay wave, the amplitude attenuation of the rectangular wave and exponential decay wave with more high-frequency components is stronger than that of the half-sine wave. The wave velocity slowness is not related directly to the incident waveform. Rock damage could enhance the high-frequency filtering function of rocks.

(4) By establishing a relationship between the damage and the rock quality index defined by wave amplitude, an improved rock quality classification for rock fracturing degree was introduced, which groups the rock into zones of slightly fractures, moderately fractured and strongly fractured.

Acknowledgements This research is financially supported by the National Key R&D Program of China (No. 2018YFC0407002), Department of Science and Technology of Guangdong Province (No. 2019ZT08G315) National Science Foundation of China (No. 51974197).

Compliance with Ethical Standards

Conflict of interest We declare that there is no conflict of interest in this paper.

References

Akkaya Y, Voigt T, Subramaniam KV, Shah SP (2003) Nondestructive measurement of concrete strength gains by an ultrasonic wave reflection method. Mater Struct 36(8):507–514

Bansal R, Sen MK (2008) Finite-difference modelling of S-wave splitting in anisotropic media. Geophys Prospect 56(3):293–312

Bass JD (1995) Elasticity of minerals, glasses, and melts. In: Mineral physics & crystallography: a handbook of physical constants. American Geophysical Union, Washington

Cadoret T, Mavko G, Zinszner B (1998) Fluid distribution effect on sonic attenuation in partially saturated limestones. Geophysics 63(1):154–160

Carpinteri A, Lacidogna G (2007) Damage evaluation of three masonry towers by acoustic emission. Eng Struct 29(7):1569–1579

Chaki S, Takarli M, Agbodjan WP (2008) Influence of thermal damage on physical properties of a granite rock: porosity, permeability and ultrasonic wave evolutions. Constr Build Mater 22(7):1456–1461

Chen S, Yue ZQ, Tham LG (2004) Digital image-based numerical modeling method for prediction of inhomogeneous rock failure. Int J Rock Mech Min Sci 41(6):939–957

Deng XF, Chen SG, Zhu JB, Zhou YX, Zhao ZY, Zhao J (2015) UDEC–AUTODYN hybrid modeling of a large-scale underground explosion test. Rock Mech Rock Eng 48(2):737–747

Duan Y, Li X, Zheng B, He J, Hao J (2019) Cracking evolution and failure characteristics of longmaxi shale under uniaxial compression using real-time computed tomography scanning. Rock Mech Rock Eng 52(2):3003–3015

Faella G, Frunzio G, Guadagnuolo M, Donadio A, Ferri L (2012) The church of the nativity in bethlehem: non-destructive tests for the structural knowledge. J Cult Herit 13(4):e27–e41

Fan LF, Wu ZJ (2016) Evaluation of stress wave propagation through rock mass using a modified dominate frequency method. J Appl Geophys 132:53–59

Fei Y (1995) Thermal expansion. In: Ahrens TJ (ed) Mineral physics and crystallography: a handbook of physical constants. American Geophysical Union, Washington

Feng J, Wang E, Chen L, Li X, Xu Z, Li G (2016) Experimental study of the stress effect on attenuation of normally incident p-wave through coal. J Appl Geophys 132:25–32

Fourmaintraux, D (1976) Characterization of rocks; laboratory tests, Chapter IV in La Mécanique des roches appliquée aux ouvrages du génie civil by Marc Panet et al. Ecole National des Ponts et Chaussées, Paris

Gonzalez RC (1997) Digital image processing, 2nd edn. Prentice Hall, New Jersey

Goodman RE (1980) Introduction to Rock Mechanics. Wiley, New York

Gu J, Zhao Z (2010) Considerations of the discontinuous deformation analysis on wave propagation problems. Int J Numer Anal Met 33(12):1449–1465

Hadjigeorgiou J, Lemy F, Côté P, Maldague X (2003) An evaluation of image analysis algorithms for constructing discontinuity trace maps. Rock Mech Rock Eng 36(2):163–179

Huang XL, Qi SW, Guo SF, Dong WL (2014) Experimental study of ultrasonic waves propagating through a rock mass with a single joint and multiple parallel joint. Rock Mech Rock Eng 47(2):549–559

Huang XL, Qi SW, Williams A, Zou Y, Zheng BW (2015) Numerical simulation of stress wave propagating through filled joints by particle model. Int J Solids Struct 69–70:23–33

Ichikawa Y, Kawamura K, Uesugi K, Seo YS, Fujii N (2001) Micro- and macrobehavior of granitic rock: observations and viscoelastic homogenization analysis. Comput Method Appl M 191(1–2):47–72

Itoh M, Kondo M, Kojima C, Jin WZ, Watanabe G, Taya K (1996) Digital image processing for aggregate orientation in asphalt concrete mixtures. Can J Civ Eng 23(2):480–489

Jaeger JC, Cook N, Zimmerman RW (2007) Fundamentals of rock mechanics. Blackwell Publ, Malden

Kachanov LM, Krajcinovic D (1986) Introduction to continuum damage mechanics. J Appl Mech 54(2):481

Kuszmaul JS (1987) A new constitutive model for fragmentation of rock under dynamic loading. In: 2nd International Symposium on Rock Fragmentation by Blasting. Keystone. Colorado. 412–423

Lei X, Masuda K, Nishizawa O, Jouniaux L, Liu L, Ma W, Kusunose K (2004) Detailed analysis of acoustic emission activity during catastrophic fracture of faults in rock. J Struct Geol 26(2):247–258

Lemaitre J, Chaboche JL (1994) Mechanics of solid materials. Cambridge University Press, New York

Li JC (2013) Wave propagation across non-linear rock joints based on time-domain recursive method. Geophys J Int 193:970–985

Li XB (2014) Rock dynamics fundamentals and applications. Science Press, Beijing

Li JC, Li HB, Jiao YY, Liu YQ, Xia X, Yu C (2014) Analysis for oblique wave propagation across filled joints based on thin-layer interface model. J Appl Geophys 102:39–46

Li JC, Li HB, Zhao J (2015) An improved equivalent viscoelastic medium method for wave propagation across layered rock masses. Int J Rock Mech Min Sci 73:62–69

Li JC, Li NN, Li HB, Zhao J (2017a) An SHPB test study on wave propagation across rock masses with different contact area ratios of joint. Int J Impact Eng 105:109–116

Li ZC, Li LC, Huang B, Zhang LY, Li M, Zuo JQ (2017b) Numerical investigation on the propagation behavior of hydraulic fractures in shale reservoir based on the dip technique. J Petrol Sci Eng 154:302–314

Liao ZY, Zhu JB, Xia KW, Tang CA (2016) Determination of dynamic compressive and tensile behavior of rocks from numerical tests of split Hopkinson pressure and tension bars. Rock Mech Rock Eng 49:3917–3934

Ma T, Yang C, Chen P, Wang X, Guo Y (2016) On the damage constitutive model for hydrated shale using CT scanning technology. J Nat Gas Sci Eng 28:204–214

Moustachi O, Thimus JF (1997) P-wave attenuation in creeping rock and system identification. Rock Mech Rock Eng 30(4):169–180

Müller TM, Gurevich B, Lebedev M (2010) Seismic wave attenuation and dispersion resulting from wave-induced flow in porous rocks-A review. Geophysics 75(5):A147–A164

Ohtsu M, Watanabe H (2001) Quantitative damage estimation of concrete by acoustic emission. Constr Build Mater 15(5–6):217–224

Persson PA (1997) The relationship between strain energy, rock damage, fragmentation, and throw in rock blasting. Fragblast 1(1):99–110

Qajar J, Arns CH (2016) Characterization of reactive flow-induced evolution of carbonate rocks using digital core analysis—part 1: assessment of pore-scale mineral dissolution and deposition. J Contam Hydrol 192:60–86

Smith AR (1978) Color gamut transform pairs. Conference on Computer Graphics and Interactive Techniques. ACM 12(12):19

Suazo G, Fourie A, Doherty J (2016) Experimental investigation of propagation and transmission of compressional stress waves in cemented paste backfill. J Geotech Geo Environ 143(3):04016104

Svitek T, Vavryčuk V, Lokajíček T, Petružálek M, Kern H (2017) Effect of pressure on 3d distribution of p-wave velocity and attenuation in antigorite serpentinite. Geophysics 82(4):1–42

Tang CA (1997) Numerical simulation of progressive rock failure and associated seismicity. Int J Rock Mech Min Sci 34(2):249–261

Tang CA, Chen ZH, Xu XH, Li C (1997) A theoretical model for Kaiser effect in rock. Pure Appl Geophys 150(2):203–215

Taylor LM, Chen EP, Kuszmaul JS (1986) Microcrack-induced damage accumulation in brittle rock under dynamic loading. Comput Method Appl M 55(3):301–320

Tuffen H, Smith R, Sammonds PR (2008) Evidence for seismogenic fracture of silicic magma. Nature 453(7194):511–514

Wang ZL, Li YC, Wang JG (2008) Numerical analysis of blast-induced wave propagation and spalling damage in a rock plate. Int J Rock Mech Min 45(4):600–608

Watanabe T, Sassa K (1996) Seismic attenuation tomography and its application to rock mass evaluation. Int J Rock Mech Min Sci Geomech Abstr 33(5):467–477

Weibull W (1951) A statistical distribution function of wide applicability. J Appl Mech 13(2):293–297

Xie H, Zhu J, Zhou T, Zhang K, Zhou C (2020) Conceptualization and preliminary study of engineering disturbed rock dynamics. Geomech Geophys Geo-Energy Geo-Resour 6:34. https://doi.org/10.1007/s40948-020-00157-x

Xue YJ, Cao JX, Wang DX, Tian RF, Shu YX (2013) Detection of gas and water using hht by analyzing p- and s-wave attenuation in tight sandstone gas reservoirs. J Appl Geophys 98(3):134–143

Yang SQ, Jing HW (2011) Strength failure and crack coalescence behavior of brittle sandstone samples containing a single fissure under uniaxial compression. Int J Fracture 168(2):227–250

Yang H, Duan HF, Zhu JB (2019) Ultrasonic P-wave propagation through water-filled rock joint: an experimental investigation. J Appl Geophys 169:1–14

Yue ZQ, Chen S, Tham LG (2003) Finite element modeling of geomaterials using digital image processing. Comput Geotech 30(5):375–397

Zhao J, Cai JG (2001) Transmission of elastic P-waves across single fractures with a nonlinear normal deformational behavior. Rock Mech Rock Eng 34(1):3–22

Zhou H, Yang X, Hu QZ, Cheng CB (2011) Strength test and mechanism of softening of chlorite schist. Chin Soil Eng Found 25(1):45–49 **(In Chinese)**

Zhou T, Zhu JB, Ju Y, Xie HP (2019) Volumetric fracturing behavior of 3D printed artificial rocks containing single and double 3D internal flaws under static uniaxial compression. Eng Fract Mech 205:190–204

Zhou T, Zhu J, Xie H (2020) Mechanical and volumetric fracturing behaviour of three-dimensional printing rock-like samples under dynamic loading. Rock Mech Rock Eng. https://doi.org/10.1007/s00603-020-02084-5

Zhu WC, Tang CA (2006) Numerical simulation of Brazilian disc rock failure under static and dynamic loading. Int J Rock Mech Min Sci 43:236–252

Zhu WC, Liu J, Yang TH, Sheng JC, Elsworth D (2006) Effects of local rock heterogeneities on the hydromechanics of fractured rocks using a digital-image-based technique. Int J Rock Mech Min Sci 43(8):1182–1199

Zhu WC, Liu J, Elsworth D, Polak A, Grader A, Sheng JC, Liu JX (2007) Tracer transport in a fractured chalk: x-ray CT characterization and digital-image-based (DIB) simulation. Transp Porous Med 70(1):25–42

Zhu JB, Deng XF, Zhao XB, Zhao J (2013) A numerical study on wave transmission across multiple intersecting joint sets in rock masses with UDEC. Rock Mech Rock Eng 46(6):1429–1442

Zhu JB, Liao ZY, Tang CA (2016) Numerical SHPB tests of rocks under combined static and dynamic loading conditions with application to dynamic behavior of rocks under in situ stresses. Rock Mech Rock Eng 49(10):3935–3946

Zhu JB, Zhou T, Liao ZY, Sun L, Li XB, Chen R (2018) Replication of internal defects and investigation of mechanical and fracture behaviour of rock using 3D printing and 3D numerical methods in combination with X-ray computerized tomography. Int J Rock Mech Min Sci 106:198–212

Zhu JB, Li H, Deng JH (2019) A one-dimensional elastoplastic model for capturing shear behaviour of joints with irregular triangular asperities based on direct shear tests and its validation. Rock Mech Rock Eng 52(6):1671–1687